Deciphering the interactions between the Bacillus cereus linear plasmid, pBClin15, and its host by high-throughput comparative proteomics

Jean-Paul Madeira, Helene Omer, Beatrice Alpha-Bazin, J. Armengaud, Catherine Duport

Journal of Proteomics (2016), Vol. 146, p. 25-33, DOI: 10.1016/j.jprot.2016.06.022
Journal homepage : www.elsevier.com/locate/jprot

Deciphering the interactions between the *Bacillus cereus* linear plasmid, pBClin15, and its host by high-throughput comparative proteomics

Jean-Paul Madeira [a,b], Hélène Omer [a,b], Béatrice Alpha-Bazin [b], Jean Armengaud [b], Catherine Duport [a,*]

[a] *SQPOV, UMR0408, Avignon Université, INRA, F-84914 Avignon, France*
[b] *CEA, DSV, IBiTec-S, SPI, Li2D, Laboratory "Innovative technologies for Detection and Diagnostics", Bagnols-sur-Cèze F-30200, France*

Keywords:
Proteome
Bacillus cereus
Plasmid
Prophage
Shotgun proteomics

A B S T R A C T

The pathogen, *Bacillus cereus*, is able to adapt its metabolism to various environmental conditions. The reference strain, *Bacillus cereus* ATCC 14579, harbors a linear plasmid, pBClin15, which displays a cryptic prophage behavior. Here, we studied the impact of pBClin15 on the aerobic respiratory metabolism of *B. cereus* by curing its host strain. We compared, by means of a high-throughput shotgun proteomic approach, both the cellular proteome and the exoproteome of *B. cereus* ATCC 14579 in the presence and absence of pBClin15 at the early, late and stationary growth phases. The results were visualized through a hierarchical cluster analysis of proteomic data. We found that pBClin15 contributes significantly to the metabolic efficiency of *B. cereus* by restricting the production of chromosome-encoded phage proteins in the extracellular milieu. The data also revealed intricate regulatory mechanisms between pBClin15 and its host. Finally, we show that pBClin15 provides benefit to its host to adapt to different ecologic niches.
Biological significance: Bacteria belonging to the *Bacillus cereus* group include *B. cereus*, a notorious food borne pathogen which causes gastroenteritis. The *B. cereus* type, strain ATCC 14579, harbors a linear plasmid, pBClin15, which displays cryptic prophage behavior. Here, we present data supporting the idea that pBClin15 may have a much greater role in *B. cereus* metabolism that has hitherto been suspected. Specifically, our comparative proteomic analyses reveal that pBClin15 manages *B. cereus* central metabolism to optimize energy and carbon utilization through the repression of several chromosome-encoded phage proteins. These results suggest that pBClin15 provides benefit to the host for surviving adverse environmental conditions.

1. Introduction

Members of the *Bacillus cereus sensu lato* group are found in diverse environments and include eight closely related species – *Bacillus cereus sensu stricto*, *Bacillus anthracis*, *Bacillus thuringiensis*, *Bacillus weihenstephanensis*, *Bacillus mycoides*, *Bacillus pseudomycoides*, *Bacillus cytotoxicus*, and *Bacillus toyonensis* [1,2]. The plasmids in this group display a strain-dependent distribution, with some strains containing no plasmid, whereas others have many. Some of these plasmids have a small genome size, only 2 kb, whereas others are very large, up to 600 kb [3]. Large plasmids are key components in defining the phenotypic traits associated with pathogenesis [4]. For example, emetic syndrome, which is associated with *B. cereus sensu stricto*, is caused by cereulide. The cereulide synthetase gene cluster, which encodes the enzymatic machinery required for the biosynthesis of cereulide, is located on a 208 kb megaplasmid [5]. As a mammalian pathogen, the ability of *B. anthracis* to cause anthrax originates from two large plasmids: pXO1 (181.6 kb) that encodes the tripartite lethal toxin complex and pXO2 (93.5 kb), which contains the biosynthetic genes for the poly-γ-D-glutamic acid capsule [6]. *B. thuringiensis* forms crystal-like parasporal inclusions during sporulation [7–9]. These inclusions contain δ-endotoxins with insecticidal properties. Most of the genes (*cry*) encoding these toxins are located on large plasmids [10]. Whereas the role of large plasmids in pathogenesis is well defined, the function of the other plasmids in the group is relatively unknown.

The *B. cereus* type, strain ATCC 14579, harbors a 15,274 bp linear plasmid, pBClin15, which displays cryptic prophage behavior [11–13]. The genetic structure of pBClin15 is reminiscent of temperate phages belonging to the *Tectiviridae* family. This family includes the bacteriophages, Bam35, GIL01 and GIL16 from *B. thuriengensis* and AP50 from *B. anthracis* [13–18]. The pBClin15 genome contains 28 open reading frames (ORFs) [17]. Some of these ORFs encode proteins involved in phage genome replication and regulation, virion structure and DNA packaging [17,19], but the function of many is so far undocumented. One of these ORFs, namely ORF2, encodes a protein (Bcp0002) that displays binding properties towards DNA fragments of both chromosomal and plasmid origin. The effect of Bcp0002 binding is currently unknown [20].

* Corresponding author at: UMR SQPOV, INRA PACA, 228, Route de l'Aérodrome, CS 40509, Domaine Saint Paul-Site Agroparc, 84914 Avignon Cedex 9, France.
E-mail address: catherine.duport@univ-avignon.fr (C. Duport).

Journal of Proteomics (2016), Vol. 146, p. 25-33, DOI: 10.1016/j.jprot.2016.06.022
Journal homepage : www.elsevier.com/locate/jprot

With the emergence of "global systems biology" tools (mainly DNA microarrays), cryptic prophages have gradually gained attention, as part of host physiology, especially under stress conditions [21]. Our goal here was to understand the importance of the effect of pBClin15 on *B. cereus* physiology under normal growth conditions. For this, bacteria were grown in pH-regulated batch cultures under fully oxic conditions. We designed a high-throughput shotgun proteomic approach to decipher the interaction of pBClin15 with its host. Hierarchical clustering analysis of the proteomic data identified the altered biological processes, according to the metabolic data, and the empirical Bayes approach identified the main regulators responsible for the changes in the phenotypes. Strikingly, we determined that pBClin15 has a beneficial impact on *B. cereus* physiology. This probably helps these bacteria to cope with adverse environments.

2. Materials and methods

2.1. Bacterial strains and growth conditions

The B. cereus strain used in this study was the reference strain, ATCC 14579 [12]. This strain was cured of pBClin15 as described by Voros et al. [21], resulting in the ΔpBClin15 strain. *B. cereus* strains (with and without pBClin15) were cultured in batches (three independent cultivations per strain) at $pO_2 = 100\%$ [22] in minimal MOD medium supplemented with 30 mM glucose as the carbon source [23]. Each batch culture was inoculated with an overnight subculture at an initial optical density at 600 nm (OD_{600nm}) of 0.02. Aerobic batch cultures were performed at 37 °C in a 3-liter bioreactor (BioFlo®/CelliGen®115, New Brunswick), with a working volume of 2 l. The pH was maintained at a controlled value of 7.2 by automatic addition of 5 M KOH. *B. cereus* growth was monitored spectrophotometrically at 600 nm.

2.2. Cellular and exoproteome extraction and metabolite assays

The cells were harvested by centrifugation at the early exponential (EE), late exponential (LE) and stationary (S) growth phases for each of the bioreactor cultures and stored frozen at −80 °C until analysis. Soluble cellular proteins were extracted as previously described [24]. The extracellular proteins were obtained by trichloroacetic acid precipitation as described in [22]. The protein concentration was determined by the Bradford protein assay after TCA precipitation. Enzymatic test kits from Roche (Meylan, France) were used to measure glucose, lactate, ethanol, formate, acetate, and succinate concentrations in the supernatants.

2.3. Proteolysis and shotgun tandem mass spectrometry

Protein samples were loaded onto NuPAGE 4–12% Bis-Tris gels (Invitrogen) for a short (about 3 mm) electrophoretic migration in denaturing conditions. For each protein sample, the whole content was extracted as a single polyacrylamide band. The bands were subjected to proteolysis with sequencing grade trypsin (Roche) using 0.01% ProteaseMAX surfactant (Promega) as previously described [25,26]. The resulting peptides were analyzed by nanoLC-MS/MS using an LTQ-Orbitrap XL hybrid mass spectrometer (ThermoFisher) coupled to an Ultimate 3000 nRSLC system (Dionex, ThermoFisher). The experimental set-up and conditions were as described [22,27]. Briefly, peptide digests were desalted on-line on a reverse-phase precolumn (Acclaim PepMap 100 C18, 5 μm bead size, 100-Å pore size, 300 μm i.d. × 5 mm, Dionex ThermoFisher). The peptides from the extracellular digests were then resolved on a nanoscale C18 PepMap100™ capillary column (3 μm bead size, 100-Å pore size, 75 μm i.d., 15 cm length, LC Packings, ThermoFisher) using a 90-min gradient. The peptides from cellular digests were resolved with the same column but 50 cm long using a 180-min gradient. In both cases, the gradient was from 4 to 40% solvent B (0.01% HCOOH, 100% CH_3CN) with solvent A being 0.01% HCOOH, 100% H_2O. Full-scan mass spectra were measured from *m/z* 300 to 1800 in data-dependent mode using the TOP3 strategy.

2.4. MS/MS spectra assignments to peptide sequences and protein validation

An in-house polypeptide sequence database was made of the sequences of all previously annotated proteins encoded by the *B. cereus* ATCC 14579 chromosome (NC_004722) and the plasmid pBClin15 (NC_004721), and 44 proteins identified by a previous proteogenomic study (see Supplementary Table 1 in Ref. [28]). This database, used to assign peptide sequences to MS/MS spectra, comprises 5299 polypeptide sequences totaling 1,464,675 amino acids. The MASCOT Daemon search engine (version 2.3.02; Matrix Science) was used for searching tryptic peptides with the following parameters: full-trypsin specificity, a mass tolerance of 5 ppm on the parent ion and 0.5 Da on the MS/MS, carboxyamidomethylated Cys (+57.0215) as a fixed modification and oxidized methionine (+15.9949) as a variable modification. The number of tolerated missed cleavages was set at 2. All peptide matches with a score below a *p*-value of 0.05 were filtered by the IRMa 1.28.0 parser [29]. A protein was considered validated when at least two different peptides were detected when considering all the samples. The false-positive rate for protein identification was estimated using the appropriate decoy database as below 0.1% with these parameters. The mass spectrometry proteomics data have been deposited in the ProteomeXchange Consortium (http://proteomecentral.proteomeexchange.org) via the

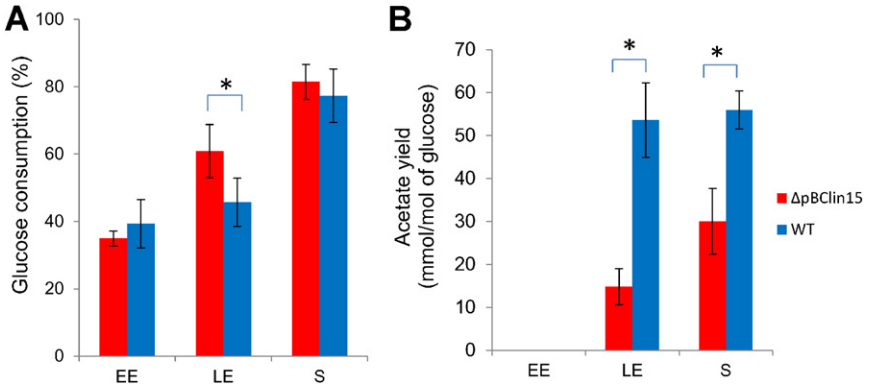

Fig. 1. Growth characteristics of ΔpBClin15 and its parental *B. cereus* ATCC 14579 strain. Panel A. Kinetics of glucose consumption in ΔpBClin15 and WT cells. Consumption of glucose was measured from the samples isolated at the EE, LE and S growth phases. Panel B. Kinetics of acetate production. Acetate yield was measured from the samples isolated at the EE, LE and S growth phases. Error bars represent the standard deviation from 3 independent measures. Significant differences (p-value < 0.05) are indicated with asterisks.

Journal of Proteomics (2016), Vol. 146, p. 25-33, DOI: 10.1016/j.jprot.2016.06.022
Journal homepage : www.elsevier.com/locate/jprot

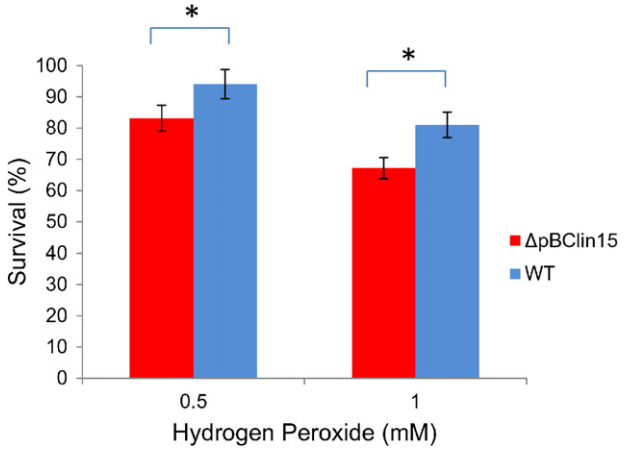

Fig. 2. Survival of ΔpBClin15 and its parental *B. cereus* ATCC 14579 strain towards external hydrogen peroxide insult. Cells were grown in liquid culture to the mid-exponential growth phase, and subjected to 0.5 and 1 mM H_2O_2, respectively. Colony forming units per mL were counted and expressed as (N/N0) × 100. Error bars represent the standard deviation from 6 independent measures. Significant differences (p-value < 0.05) between ΔpBClin15 and wild-type (WT) cells are indicated with asterisks.

PRIDE partner repository (http://www.ebi.ac.uk/pride) with the dataset identifiers, PXD001568, PXD002788 and PXD002789.

2.5. Spectral count-based protein quantification and statistical analysis

The number of MS/MS spectra per protein (spectral counts) was extracted in the 3 different nanoLC-MS/MS biological replicates for each growth phase. The normalized spectral abundance factor (NSAF) for each protein was calculated by dividing the number of spectral count (SC) by the polypeptide length (L) and by the sum of SC/L for all N proteins in the experiment [30]. Hierarchical clustering analysis (HCA) was carried out with biological replicates of each growth phase as individuals and the NSAF values assigned to functional groups as quantitative variables. The data analyses were performed with Pvclust, a package written in R (https://cran.r-project.org/bin/windows/base/old/3.2.0/) for assessing the uncertainty in HCA [31]. Pvclust provides a dendrogram that assembles all elements into a single tree with two types of p-values: Approximately Unbiases (AU) p-value, which is computed by multiscale bootstrap resampling, is a better approximation to unbiased p-value than Bootstrap Probability (BP) value computed by normal bootstrap resampling. One can consider that clusters (edges) with high AU values (e.g. 95%) are strongly supported by data. A colored representation of the primary data table was carried out with the R package MADE4 [32] and appended to the dendrogram to indicate the nature of the computed relationship among functional groups in the table [33]. Analyses of abundance level change of proteins were performed with the LIMMA package by the LIMMA Voom method [34], a package written in R dedicated to linear models for microarrays. The Voom transformation was applied to the spectral counts of each protein. After this transformation, the protein abundances from label-free quantitative proteomics can be analyzed as if they were microarray data, and linear modeling may apply. To determine the differential abundance factors of proteins, the trimmed mean of M-values (TMM) normalization method was applied. After Voom transformation and TMM normalization, quantitative proteomics data were analyzed by empirical Bayes moderation of the standard errors towards a common value. Results include ($\log_2$) fold changes (FC), the average $\log_2$-abundance level for

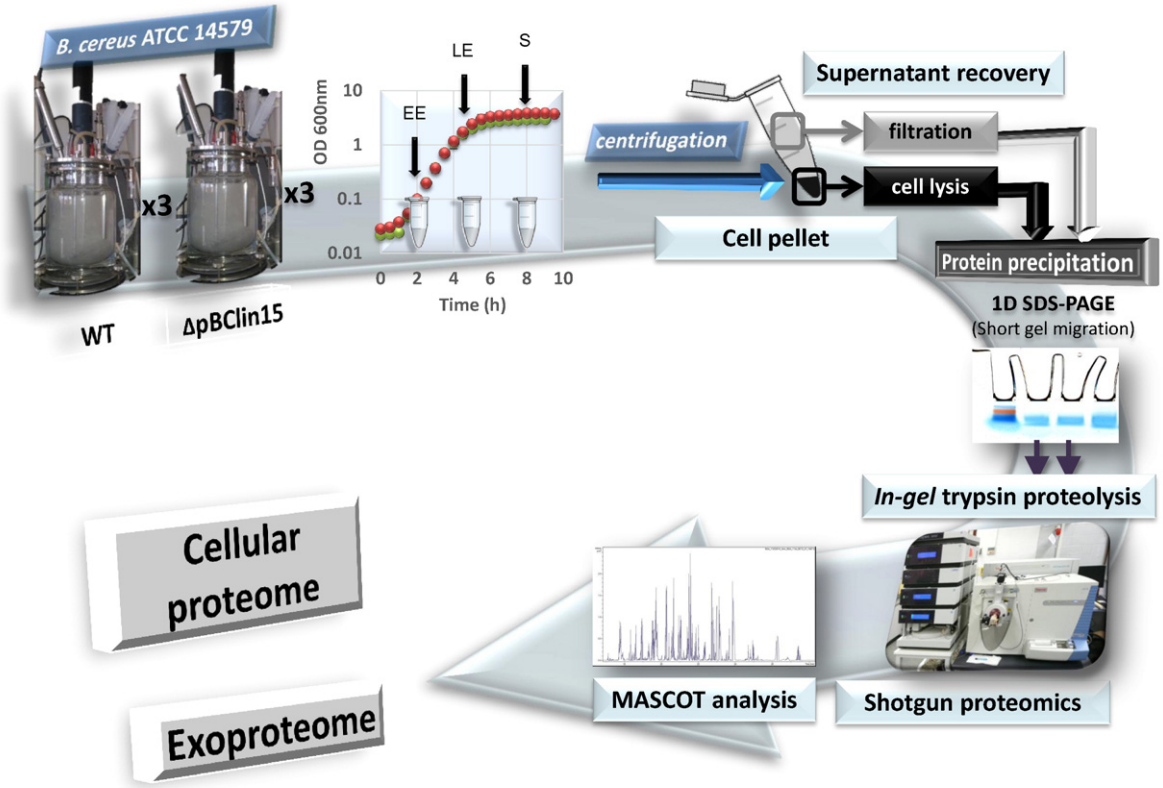

Fig. 3. Schematic description of the comparative analysis of ΔpBClin15 and *B. cereus* ATCC 14579 proteomic profiles. Cellular and extracellular samples were harvested at the early exponential (EE), late exponential (LE) and stationary (S) growth phases and separated by centrifugation. Protein samples were separated by one-dimensional (1D) polyacrylamide gel electrophoresis (PAGE). Proteins were converted into a set of peptides by trypsin digestion. Peptide mixtures were analyzed by shotgun proteomics. Peak lists were generated with the MASCOT software. Cellular and extracellular proteins were identified using an in-house polypeptide sequence database containing the sequences of all annotated proteins encoded by the *B. cereus* chromosome (NC_004722) and pBClin15 plasmid (NC_004721). See text for further details on strategy.

Journal of Proteomics (2016), Vol. 146, p. 25-33, DOI: 10.1016/j.jprot.2016.06.022
Journal homepage : www.elsevier.com/locate/jprot

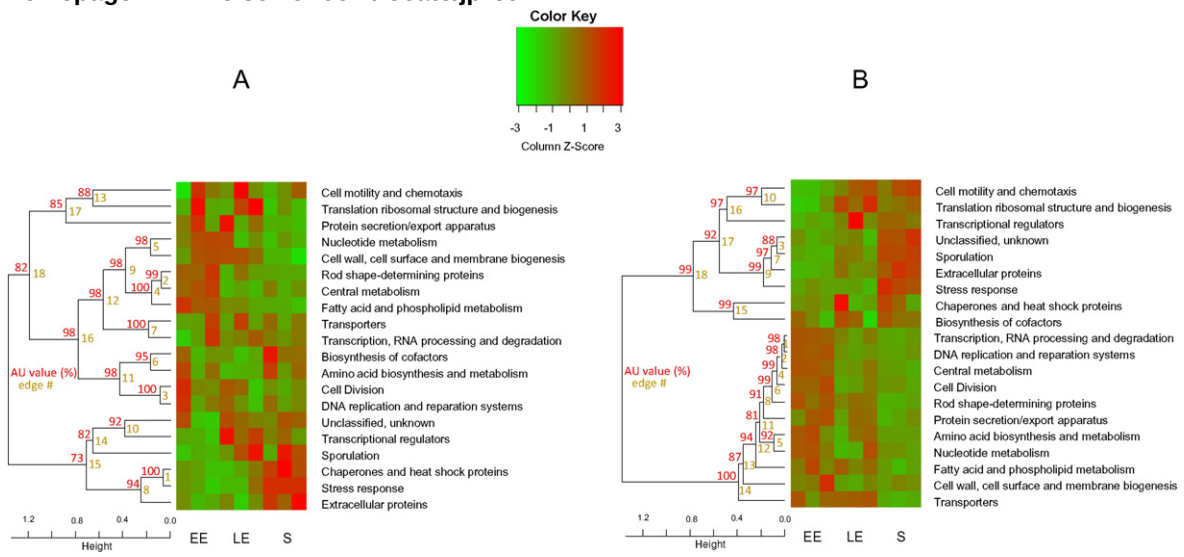

Fig. 4. Hierarchical clustering of cellular proteome dynamics based on functional group profiles. Panel A. HCA from *B. cereus* ATCC 14579 proteomic data. Panel B. HCA from ΔpBClin15 proteomic data. Detailed composition of the 20 functional groups is given in Supplementary Table S3. The dendrograms and heat maps were constructed as described in the Material and methods. Values on the edges (clusters) of the clustering are AU *p*-values (%). The colored scale in the heatmaps ranges from saturated green for column *z*-score −2 to saturated red for column *z*-score 2. Each functional group is represented by a single row of colored boxes. Each growth phase is represented by 3 columns, which correspond to the 3 biological replicates.

each protein across all samples, *t*-statistics, *p*-values, *p*-value adjusted for multiple testing, and *B*-statistics.

2.6. MS signal based data analysis using MaxQuant

The mass spectrometry raw data were processed by MaxQuant software (version 1.5.3.30) [35] using Andromeda [36] for peptide search against the in-house database of 5299 polypeptide sequences. For database searches default settings were used, with the additional options "match between run" and Label-Free Quantification (LFQ) [37] selected for the quantification purpose. The statistical analysis was performed with Perseus (version 1.5.1.2.6, standard parameters) on the logarithmized normalized ratio (base 2). Results include ($\log_2$) LFQ and *t*-statistics.

2.7. Hydrogen peroxide killing assay

B. cereus strains (with and without pBClin15) were grown to mid-log phase (OD_{600} ~ 0.3) in MOD medium supplemented with 30 mM glucose. The cells were then centrifuged and resuspended in an equal volume of phosphate-buffered saline solution (PBS). Hydrogen peroxide responses were assessed by exposing samples 20 min to 0.5 mM and 1 mM H_2O_2, respectively. Aliquots (100 µl) of the samples were diluted in H_2O, appropriate dilutions of the culture were plated onto LB

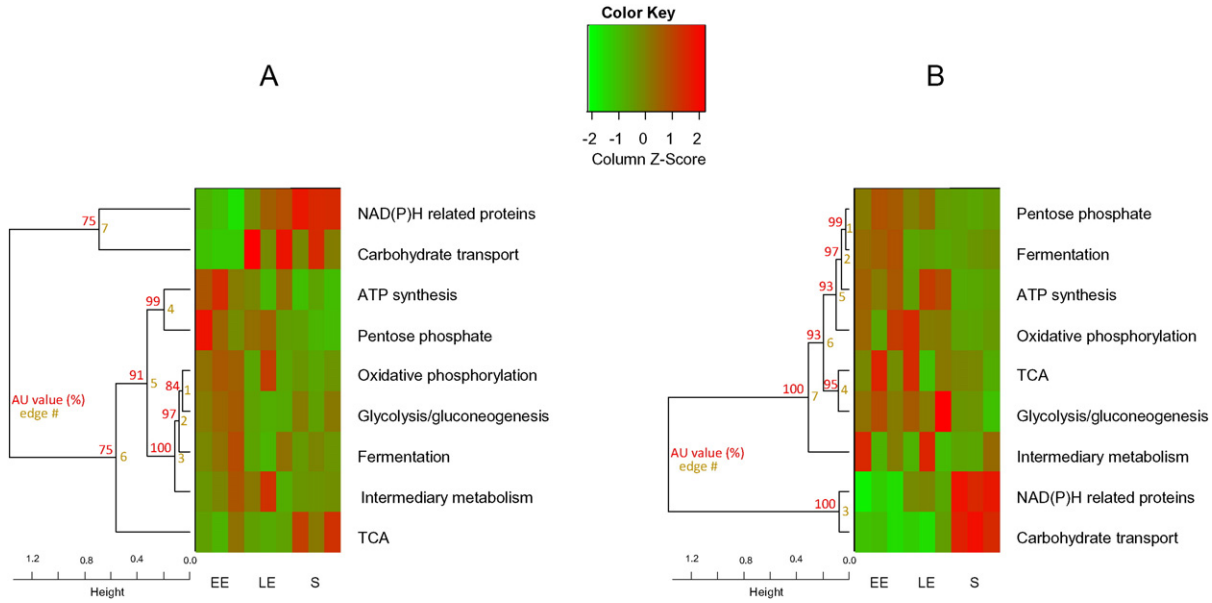

Fig. 5. Comparative analysis of central metabolism-related protein dynamics. Proteins classified in the central metabolism group were subcategorized into 9 subgroups (see Table S3 for details). Hierarchical clustering analysis of the 9 central metabolism-related subgroups in WT (Panel A) and ΔpBClin15 (Panel B), respectively. The dendrograms and heat maps were constructed as described in the Material and Methods. Values on the edges (clusters) of the clustering are AU *p*-values (%). The colored scale in the heatmaps ranges from saturated green for column *z*-score − 2 to saturated red for column *z*-score 2. Each functional group is represented by a single row of colored boxes. Each growth phase is represented by 3 columns, which correspond to the 3 biological replicates.

Journal of Proteomics (2016), Vol. 146, p. 25-33, DOI: 10.1016/j.jprot.2016.06.022
Journal homepage : www.elsevier.com/locate/jprot

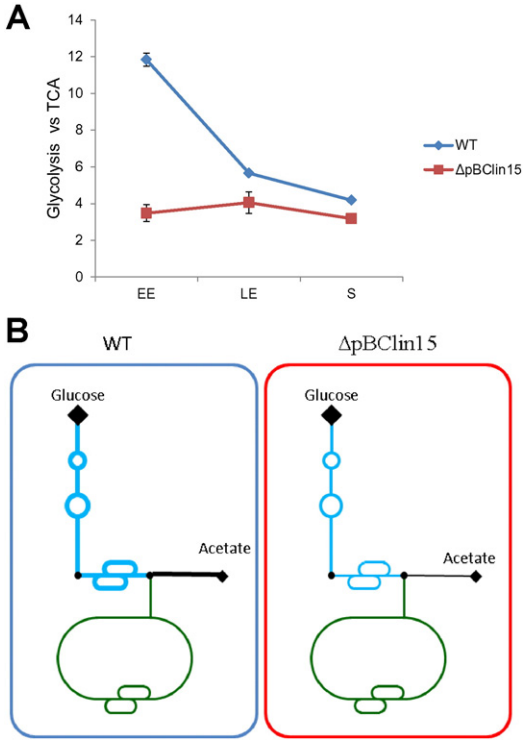

Fig. 6. Focus on glycolysis/gluconeogenesis and TCA pathways based on proteomic profiles. Panel A. Dynamics of proteins categorized in glycolysis/gluconeogenesis and TCA in *B. cereus* ATCC 14579 (WT) and ΔpBClin15. Panel B. Simplified overviews of the main central metabolic pathways in WT and ΔpBClin15. Line width and font size indicate low or high protein levels based on NSAF. Acetate excretion, which was quantified, is shown. Glycolysis is represented in blue and TCA is indicated in green.

agar, and after overnight incubation at 37 °C the colony forming units (CFUs) were counted. All the experiments were performed at least in triplicate, and at least 2 technical replicates from each dilution step were carried out to determine the number of CFUs.

3. Results and discussion

3.1. Growth characteristics of the B. cereus ATCC 14579 and ΔpBClin15 (pBClin15-cured) strains

A pBClin15-cured *B. cereus* ATCC 14579 strain, named ΔpBClin15, was constructed as described by Voros et al. [21]. The removal of pBClin15 was confirmed by PCR. The ΔpBClin15 and wild-type strains were grown in pH-regulated batch cultures (pH 7.2) on MOD medium supplemented with 30 mM glucose as the carbon source, under full aerobiosis ($pO_2 = 100\%$). Supplementary Fig. 1 in Ref. [28] reports the growth curves of both strains. Despite an extended lag time (1.9 ± 0.2 *vs* 0.6 ± 0.6), ΔpBClin15 cells started exponential growth at a rate comparable to that of the wild-type ($\mu_{max} = 1.7 \pm 0.3\ h^{-1}$). However, they reached the stationary growth phase at a higher final density ($OD_{600nm} = 3.8 \pm 0.4$) than the wild-type cells ($OD_{600nm} = 2.9 \pm 0.0$). These observations suggest that ΔpBClin15 had a growth advantage over the wild-type strain; in other words pBClin15 placed some burden on its host. During aerobic respiratory growth, acetate is the major by-product of glucose catabolism in *B. cereus* [23]. Fig. 1A and B show the kinetics of glucose consumption and acetate excretion, respectively, during growth. ΔpBClin15 consumed higher glucose quantities than its parental strain during the exponential growth phase (Fig. 1A) and excreted less acetate (Fig. 1B). At the end of growth, ΔpBClin15 and WT cells consumed a similar amount of glucose (Fig. 1A). These results indicate that glucose supported a higher glycolytic flux (glucose uptake), lower acetate overflow and higher final growth yield (in term of final biomass per mole of glucose) in ΔpBClin15 than in the wild-type strain [38–40]. pBClin15 thus impacts glucose catabolism in *B. cereus*.

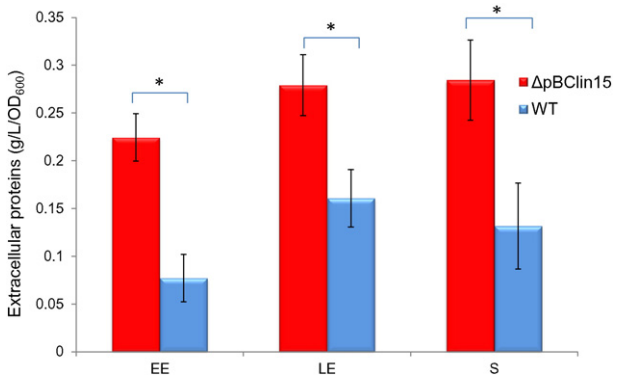

Fig. 7. Specific production of extracellular proteins by ΔpBClin15 and its parental strain. Proteins were measured from culture supernatants harvested at the early exponential (EE), late exponential (LE) and stationary phases (S). Error bars represent the standard deviation from 3 independent measures. Significant differences (p-value < 0.05) between ΔpBClin15 and wild-type cells are indicated with asterisks.

Perturbation of glucose catabolism modifies endogenous ROS production in aerobically grown bacteria. Increased endogenous ROS production can translate into increased killing by oxidants [41]. To evaluate the impact of pBClin15 on *B. cereus* tolerance to oxidant, *B. cereus* cells were exposed to hydrogen peroxide. Fig. 2 shows that ΔpBClin15 cells were more susceptible to H_2O_2 killing. Cells devoid of pBClin15 could thus experience more endogenous oxidative stress than wild-type cells.

3.2. Comparative proteomics strategy & global features

To explore the molecular impact of pBClin15 on its host, we analyzed the soluble total proteome as well as the proteins found in the extracellular environment of the cells, the so-called exoproteome [42]. Shotgun comparative proteomics was carried out by means of a label-free strategy on cells harvested by centrifugation on the first hand and on proteins present in the supernatants on the other. Fig. 3 shows the comparative proteomics strategy. Three biological replicated cultures were performed for wild-type and ΔpBClin15 cells grown in pH- and pO_2-controlled batch cultures. As indicated in Fig. 3, three samples were taken at the time points corresponding to the early exponential growth phase (EE), late exponential growth phase (LE), and stationary phase (S). From the 18 resulting samples, all of the cellular soluble proteins and exoproteins obtained after trichloroacetic acid precipitation were processed separately by means of a standard gel-based procedure for trypsin proteolysis [43]. The 36 resulting peptide fractions corresponding to these proteomes were analyzed by high-throughput tandem mass spectrometry [25]. For the cellular proteomes, a total of 242,671 MS/MS spectra were detected. Among these, 129,791 were assigned to a peptide sequence (see Supplementary Table 2 in Ref. [28]), resulting in the identification of 8452 unique peptide sequences and the quantitative monitoring of 933 proteins certified with at least two different peptides (see Supplementary Table 3 in Ref. [28]). Regarding exoproteins, a total of 49,666 MS/MS spectra were assigned (see Supplementary Table 4 in Ref. [28]) from the 97,175 spectra recorded. In this case, a total of 377 proteins were validated with at least two different peptides and their quantities were monitored (see Supplementary Table 5 in Ref. [28]). Supplementary Tables 3 and 5 in Ref. [28] present the list of these proteins categorized into 20 and 9 functional large groups, respectively [44]. The exoproteome comprises 92 proteins that were not detected and validated in the cellular proteome. When considering both datasets, a total of 1025 proteins were validated and monitored for assessing the pBClin15-dependent changes in protein abundance. These changes based on spectral counting were tested

statistically by empirical Bayes moderation of the analyzed standard errors towards a common value with the LIMMA R package [45]. They are presented in Supplementary Tables 6 and 7 in Ref. [28] as $\log_2$ of the ratio of protein abundance in ΔpBClin15 relative to that measured for the wild-type cells.

3.3. Detailed analysis of the whole cell proteome

We first examined the group behavior of cellular proteins during growth. Cellular proteins were categorized into 20 functional groups that define the principal biological processes encoded by the *B. cereus* ATCC 14579 genome [12,44]. HCA was carried out to cluster functional groups with similar time-course dynamics in wild-type and ΔpBClin15. The results of HCA are displayed as dendrograms, together with the ordered heat maps that reflect the original experimental observations (Fig. 4). Fig. 4 shows a strong difference in the clustering of functional groups in WT (Fig. 4A) and ΔpBClin15 (Fig. 4B). This indicates that pBClin15 modulates the dynamics of biological processes at the proteome level. Specifically, the dendrograms show a higher partitioning of functional groups in WT compared to ΔpBClin15, suggesting that pBClin15 may increase the propensity of the primary metabolism network to organize into nearly-independent regulation units [46]. This probably allows bacteria to use nutrients more efficiently and conserve energy to adapt to starvation conditions such as those encountered at the end of growth. Adaptation to starvation conditions involves a wide array of regulatory responses, requires high-level synthesis of proteins related to detoxification and repair systems (e.g., stress), is accompanied by a higher rate of synthesis of extracellular proteins and precedes sporulation. All of these biological processes are closely associated in ΔpBClin15 (edge 18 in Fig. 4B).

We then focused on central metabolism, which provides energy, cofactor regeneration and building blocks (nucleic acids and amino acids) for biomass synthesis and controls the extent and nature of extracellular protein expression. We subdivided the central metabolism functional group into 9 subgroups and conducted a second HCA analysis. Fig. 5 shows a breakdown of the central metabolism groups into 7 edges, which are differentially partitioned and formed in the two strains. This indicates a significant impact of pBClin15 on different pathways of central metabolism during growth. Specifically, HCA clustered glycolysis/gluconeogenesis group proteins with TCA group proteins (edge 4) with an AU *p*-value of 95% in ΔpBClin15 (Fig. 5B). This indicates that the time-course dynamics of glycolytic/gluconeogenesis and TCA group proteins were similar in ΔpBClin15. Interestingly, we noted that ΔpBClin15 sustained a lower level of glycolytic/gluconeogenesis

Table 1
Top 12 cellular proteins showing abundance-level change in ΔpBClin15 *vs* WT in the EE, LE and S growth phases, as ranked by the *B*-statistics with more details given in Table S6 [28]. The results from quantification based on MS signal analysis by MaxQuant software are given for these proteins in the last two columns.

Growth phase	Name	Protein	Gene	Functional annotation	Spectral count			MS signal	
					$\log_2$ FC [a]	Adj.[b] *p*-value	*B*[c]	$\log_2$ LFQ[d]	*t*-test Significance[e]
	BCp0002	NP_829890	BCp0002	pBClin15 encoded protein	−6.95	2.00E-22	46.12	−8.31	+
EE	RpoC	NP_830004	BC0123	DNA-directed RNA polymerase subunit β'	6.18	4.42E-11	20.04	3.52	+
	RpoB	NP_830003	BC0122	DNA-directed RNA polymerase subunit β	5.74	8.07E-10	16.91	4.03	+
	Tpx	NP_834345	BC4639	Thiol peroxidase	−4.47	4.90E-07	10.53	−3.14	+
	TegA	NP_835080	BC5419	Acetylglucosaminyldiphosphoundecaprenol *N*-acetyl-beta-D-mannosaminyltransferase	−4.5	4.90E-07	10.42	−2.92	+
	BC4791	NP_834493	BC4791	Carbonic anhydrase	−4.61	7.92E-07	9.79	−2.99	+
	FusA	NP_830008	BC0128	Elongation factor G	4.18	1.20E-06	9.27	3.08	+
	Tig	NP_834192	BC4480	Trigger factor	4.94	2.77E-06	8.31	2.95	+
	DeaD2	NP_830127	BC0259	ATP-dependent RNA helicase	4.88	2.95E-06	8.14	3.77	+
	BC4157	NP_833872	BC4157	Branched-chain alpha-keto acid dehydrogenase subunit E2	4.77	3.79E-06	7.75	3.23	+
	AspS	NP_834109	BC4397	Aspartyl-tRNA synthetase	4.7	3.79E-06	7.64	2.19	+
	Apt	NP_834114	BC4402	Adenine phosphoribosyltransferase	−4.25	3.79E-06	7.6	−1.60	+
LE	BCp0002	NP_829890	BCp0002	pBClin15 encoded protein	−6.9	1.56E-06	11.49	−9.42	+
	SufB	NP_834650	BC4979	ABC transporter-associated protein	5.96	2.56E-05	8.41	6.54	+
	BC1376	NP_831157	BC1376	Flavodoxin	−5.6	2.56E-05	8.15	−4.35	+
	ClpX	NP_834191	BC4479	ATP-dependent protease	5.24	3.60E-05	7.53	4.59	+
	RrpsA	NP_831277	BC1498	30S ribosomal protein S1	5.23	4.12E-05	7.16	4.04	+
	BC3898	NP_833618	BC3898	Integral membrane protein	−4.94	4.12E-05	7.02	−3.39	+
	BC4157	NP_833872	BC4157	Branched-chain alpha-keto acid dehydrogenase subunit E2	5.72	4.12E-05	6.95	6.70	+
	PurL	NP_830168	BC0329	Phosphoribosylformylglycinamidine synthase II	5.54	4.83E-05	6.67	5.39	+
	GlmS	NP_830058	BC0190	D-Fructose-6-phosphate amidotransferase	5.17	6.99E-05	6.01	6.32	+
	RocA	NP_830183	BC0344	1-Pyrroline-5-carboxylate dehydrogenase	5.69	6.99E-05	5.96	5.57	+
	CutC	NP_832817	BC3071	Copper homeostasis protein	−4.64	6.99E-05	5.91	−3.69	+
	DacC	NP_829918	BC0014	D-Alanyl-D-alanine carboxypeptidase	4.57	6.99E-05	5.84	5.15	+
S	BCp0002	NP_829890	BCp0002	pBClin15 encoded protein	−7.49	1.12E-03	5.47	−10.49	+
	FlaB	NP_831435	BC1658	Flagellin	3.3	1.77E-02	2.55	1.03	+
	RpmJ	NP_830034	BC0155	50S Ribosomal protein L36	−3.24	1.77E-02	2.05	1.02	+
	BC3312	NP_833051	BC3312	3-Oxoadipate enol-lactonase	3.19	1.77E-02	1.99	1.17	+
	BC2311	NP_832074	BC2311	4′-Phosphopantetheinyl transferase	−3.99	3.79E-02	0.87	−1.85	+
	FeoB	NP_830520	BC0708	Ferrous iron transport protein B	−1.76	3.79E-02	0.68	−0.28	+
	BC4042	NP_833760	BC4042	3-Hydroxyisobutyrate dehydrogenase	−3.07	3.79E-02	0.55	−2.37	+
	CwlF	NP_829909	BCp0021	*N*-Acetylmuramoyl-L-alanine amidase	−2.49	3.79E-02	0.38	−3.59	+
	BioB	NP_833832	BC4114	Biotin synthase	−2.54	3.79E-02	0.36	−3.17	+
	FabZ	NP_834943	BC5280	(3R)-Hydroxymyristoyl-ACP dehydratase	−2.32	3.79E-02	0.3	−2.23	+
	PheS	NP_834267	BC4561	Phenylalanyl-tRNA synthetase subunit α	−2.32	3.79E-02	0.3	−1.75	+
	CutC	NP_832817	BC3071	Copper homeostasis protein	−3.85	3.79E-02	0.21	−1.26	+

[a] FC: fold-change.
[b] Adj. *p*-value is the *p*-value adjusted for multiple testing.
[c] *B*-statistic (B) is the log-odds that the protein is differentially expressed.
[d] LFQ: Label-Free Quantification.
[e] *t*-test Significant: + indicates that *p*-value is below FDR (False Discovery Rate) threshold of 0.05.

Journal of Proteomics (2016), Vol. 146, p. 25-33, DOI: 10.1016/j.jprot.2016.06.022
Journal homepage : www.elsevier.com/locate/jprot

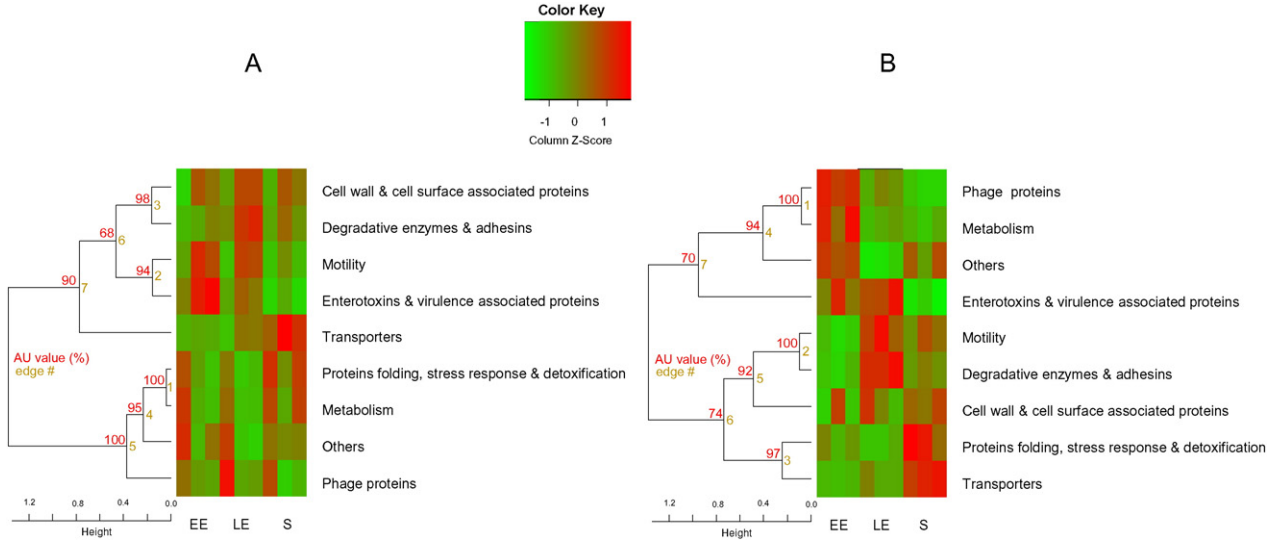

Fig. 8. Comparative analysis of exoproteome dynamics based on proteomic profile of functional groups. HCA based on 9 functional groups in *B. cereus* ATCC 14579 WT (Panel A) and ΔpBClin15 (Panel B), respectively. Detailed composition of the 9 functional groups is given in Table S5. The dendrograms and heat maps were constructed as described in the Material and Methods. Values on the edges (clusters) of the clustering are AU *p*-values (%). The colored scale in the heatmaps ranges from saturated green for column *z*-score −2 to saturated red for column *z*-score 2. Each functional group is represented by a single row of colored boxes. Each growth phase is represented by 3 columns, which correspond to the 3 biological replicates.

Table 2
List of exoproteins showing abundance-level change in ΔpBClin15 *vs* WT in the EE, LE and S growth phases, as ranked by the *B*-statistics with details given in Table S7 [28]. The results from quantification based on MS signal analysis by MaxQuant software are given for these proteins in the last two columns.

					Spectral counts			MS signal	
Growth phase	Name	Protein	Gene	Functional annotation	log_2FC [a]	Adj.[b] *p*-value	*B*[c]	log_2 LFQ[d]	*t*-test Significance[e]
EE	BC1894	NP_831667	BC1894	Phage protein	5.96	4 3E-06	9.9	9.05	+
	BCp0002	NP_829890	BCp0002	pBClin15 encoded protein	−5.38	5 5E-05	6.89	−6.88	+
	BC1893	NP_831666	BC1893	Phage protein	4 8	2.63E-04	5 2	7.57	+
	BC1862	NP_831635	BC1862	Phage protein	3.41	4.59E-03	2 3	5.68	+
	BC1911	NP_831682	BC1911	*N*-acetylmuramoyl-L-alanine amidase	3.5	1.68E-02	0.65	6.94	+
	BC1901	NP_831673	BC1901	Phage protein	3.42	1.68E-02	0.52	7.61	+
LE	CspB	NP_833272	BC3539	Cold shock protein	5.28	1.25E-10	19.82	2.37	+
	BC1893	NP_831666	BC1893	Phage protein	3.53	6.45E-05	6.33	7.57	+
	FlaA	NP_831434	BC1657	Flagellin	−2.56	7.74E-05	5.47	−1.01	+
	FlaB	NP_831435	BC1658	Flagellin	2.65	1.79E-02	0.2	0.31	+
S	BCp0010	NP_829898	BCp0010	pBClin15 encoded protein	−5.02	1.02E-03	4.38	−7.11	+
	GlmM	NP_830056	BC0188	Phosphoglucosamine mutase	−4.55	1.02E-03	4.16	−4.16	+
	BC2078	NP_831846	BC2078	Membrane Spanning Protein	3.74	3.02E-03	2.58	0.97	+
	BC4985	NP_834656	BC4985	ABC transporter substrate-binding protein	4.5	3.02E-03	2.48	1.67	+
	RocA	NP_830183	BC0344	1-Pyrroline-5-carboxylate dehydrogenase	−4.52	3.02E-03	2.34	−3.06	+
	BCp0002	NP_829890	BCp0002	pBClin15 encoded protein	−4.45	4 2E-03	1.82	−7.70	+
	CspB	NP_833272	BC3539	Cold shock protein	5.7	4 2E-03	1.78	1.70	+
	LppC	NP_834220	BC4511	Acid phosphatase	3 3	4 2E-03	1.48	4.10	+
	TgC	NP_831760	BC1991	Putative murein endopeptidase	−0.46	3.02E-03	1.4	−0.10	+
	BC1903	NP_831675	BC1903	Phage protein	2.97	4 2E-03	1.4	2.04	+
	BC3728	NP_833453	BC3728	DNA-binding protein HU	2.88	4 2E-03	1.35	2.64	+
	RpmE2	NP_834993	BC5331	50S Ribosomal protein	2.95	4 2E-03	1.34	2.77	+
	Asd	NP_833521	BC3799	Aspartate-semialdehyde dehydrogenase	−3.36	4 2E-03	1.32	0.75	+
	DnaK	NP_834024	BC4312	Molecular chaperone	−4.04	4 8E-03	1.26	−4.18	+
	Rpe	NP_833579	BC3858	Ribulose-phosphate 3-epimerase	−2.75	4.47E-03	1 11	−2.48	+
	Prc	NP_834848	BC5184	Carboxyl-terminal protease	3.31	4.52E-03	1.06	2.38	+
	TerD1	NP_830282	BC0443	Tellurium resistance protein	−3.38	4.80E-03	0.93	−1.68	+
	DltD	NP_832595	BC2846	Protein dltD precursor	3.01	6.27E-03	0.63	1.79	+
	TrpB	NP_831021	BC1237	Tryptophan synthase subunit beta	−3.74	6.48E-03	0.54	−3.28	+
	FtsL	NP_833637	BC3917	Cell division protein	2.49	8.50E-03	0.22	2.80	+
	BC4371	NP_834083	BC4371	Putative FMN-dependent NADH-azoreductase 1	3.38	8.50E-03	0.1	5.19	+
	VanW	NP_833266	BC3533	Vancomycin B-type resistance protein	4.01	8.50E-03	0.1	1.80	+
	PtsH	NP_833767	BC4049	Phosphocarrier protein HPr	2.91	8.69E-03	0.07	4.31	+

[a] FC: fold-change.
[b] Adj. *p*-value is the *p*-value adjusted for multiple testing.
[c] *B*-statistic (B) is the log-odds that the protein is differentially expressed.
[d] LFQ: Label-Free Quantification.
[e] t-test Significant: + indicates that *p*-value is below FDR (False Discovery Rate) threshold of 0.05.

proteins and higher level of TCA proteins than WT at EE growth phase (See Supplementary Table 3 in Ref. [28]). As a result, the ratio of glycolysis/gluconeogenesis *vs* TCA proteins was markedly higher in WT cells compared with ΔpBClin15 cells in the EE growth phase (~2.5-fold, Fig. 6A). Taken together, these data suggest that by disconnecting the regulation of glycolytic and TCA enzymes, pBClin15 does allow efficient coupling between glycolysis and TCA. This probably leads to higher acetate accumulation in wild-type cells, as illustrated in Fig. 6B [47,48]. Production of acetate wastes carbon that might otherwise be directed towards protein synthesis through TCA intermediates. Proteins are either used for biomass synthesis or exported. To determine whether ΔpBClin15 produced higher levels of extracellular proteins, we measured the concentration of proteins in cell supernatants. Fig. 7 shows that ΔpBClin15 produced higher levels of exoproteins than wild-type cells during growth. Biosynthesis and export of proteins require energy (ATP), which is not available for cellular oxidative damage repair systems. This could lead to a significant increase in macromolecule damage. Accordingly, we found that ΔpBClin15 exhibited (i) a significant increase in lag phase, which represents the rejuvenation of bacterial life that accompanies the repair of oxidative damage [49], and (ii) a decreased tolerance to exogenous oxidant [41,50]. Finally, by increasing the modularity of central metabolic pathways, pBClin15 may increase the ATP-dependent ability of the cell to repair the damage caused by endogenous oxidative stress during aerobic growth and increase the cell's ability to cope with additional oxidative stress.

Next, we examined the abundance-level changes of individual proteins in ΔpBClin15 *vs* WT in each growth phase (see Supplementary Table 6 in Ref. [28]) to identify the main contributors to metabolic changes. The *B*-statistical analysis uncovered a total of 58, 90 and 12 differentially expressed proteins in the EE, LE, and S growth phases, respectively (*B*-value > 0). Table 1 shows the top 12 proteins showing significant abundance level changes in the EE, LE and S growth phases, as ranked by the *B*-statistics [45]. The top protein in the three growth phases is the abundant pBClin15-encoded protein, Bcp0002, which is absent in ΔpBClin15, as expected. In the EE growth phase, the β and β′ subunits of RNA polymerase (RpoC and RpoB) stand out clearly from the other chromosome-encoded proteins both in terms of $\log_2$ (fold-change) and *B*-value ($\log_2 > 5$ and *B*-value > 16) and in terms of $\log_2$ (Label-Free quantification) (Table 1). An increase in their abundance level in ΔpBClin15 compared to WT probably increased RNA polymerase availability. This may contribute to the deregulation of growth at the expense of maintenance and damage protection [51,52]. In the LE and S growth phases, the *B*-statistics did not clearly separate the top proteins from the others (Table 1). However, LE sustained higher abundance-level change than the S growth phase, both in terms of number of proteins and fold-changes. Interestingly, we noted that the complete list of differentially expressed proteins in LE (See Supplementary Table 6 in Ref. [28]) includes the LexA repressor, which was downregulated ($\log_2$FC = −3.9, *B*-value = 3.73) in ΔpBClin15, the catabolite control protein A (CcpA), which was upregulated ($\log_2$ FC = 3.4, *B*-value = 2.72) and the transcriptional regulator, TenA ($\log_2$ FC = −3.9, *B*-value = 0.79). LexA represses the SOS response to DNA damage and regulates the lytic switch in the *Bacillus thuriengensis* temperate phage, GIL01 [19]. CcpA plays a major role in the coordinated regulation of catabolism and anabolism to ensure optimum cell propagation [53]. It also plays a key role in toxin gene expression and virulence [54]. TenA regulates the production of extracellular proteases in *Bacillus subtilis* [55]. Therefore, regulatory changes induced by pBClin15 may occur mainly at the transcriptional level through RNA polymerase availability during growth and several regulatory circuits at the end of growth.

3.4. Detailed analysis of the exoproteome

We showed that pBClin15 restricted the production of extracellular proteins, in terms of quantities. To determine whether pBClin15 also modulated the composition of the *B. cereus* exoproteome, we first compared the group behavior of exoproteins in ΔpBClin15 and its parental strain during growth. Fig. 8 (Panels A and B) shows that pBClin15 influences the hierarchical organization of functional groups during growth. Interestingly, the dendrograms revealed that (i) the dynamics of metabolism group proteins is very similar to the dynamics of phage group proteins in ΔpBClin15 (edge 1, AU *p*-value = 100%, Fig. 8B), while it was very similar to the dynamics of the folding, stress response and detoxification group proteins in WT (edge 1, AU *p*-value = 100%, Fig. 8A); this suggests a disorganization of the intracellular metabolism in pBClin15 [22], (ii) the enterotoxin/virulence-associated protein group is in the immediate vicinity of the motility and to a lesser extent the degradative enzyme & adhesins group in WT (Fig. 8A), while it was far from these groups in pBClin15 (Fig. 8B); this suggests a less efficient coordination of virulence factor secretion in ΔpBClin15. Comparison of heatmaps reveals a coordinate enrichment of metabolism and phage proteins in the EE growth phase compared with the LE and S growth phases in ΔpBClin15. Table 2 shows that the enrichment in phage proteins in EE was mainly due to the overexpression of 4 phage proteins of unknown function: BC1894, BC1893, BC1862, and BC1901. Table 2 also shows that in the EE growth phase, the pBClin15-encoded protein, Bcp0002, was at the top of the list as ranked by the *B*-statistics and was downregulated in the ΔpBClin15 exoproteome as in the cellular proteome. In the LE growth phase, the top protein in terms of fold-change and *B*-value was the cold-shock protein, CspB. Interestingly, CspB shows some sequence similarities with Bcp0002 [20]. The S growth phase supports the largest list of differentially expressed proteins with, at the top of the list, the pBClin15-encoded protein, Bcp0010, which is downregulated as expected. Taken together these data suggest that pBClin15 influences the dynamics of the *B. cereus* exoproteome by restricting the production of chromosome-encoded phage proteins through cellular regulatory circuits.

4. Conclusion

To our knowledge, this paper reports the first proteomic approach to deciphering the interaction between a cryptic prophage and its host under normal growth conditions. Our results demonstrate the beneficial impact of pBClin15 on *B. cereus* metabolism during respiratory aerobic growth. Intricate regulatory networks, including positive or negative regulation by transcriptional regulators and RNA polymerase regulation, may explain the dynamic nature of the pBClin15 interaction with its host. The pBClin15-encoded DNA-binding protein, Bcp0002, which was expressed constitutively during growth, may play an important role in this regulatory network, which needs to be investigated.

The beneficial impact of pBClin15 on *B. cereus* metabolism includes protection from oxidative damage. This helps the bacteria to cope with adverse environments [21]. This may also increase genetic stability by limiting high-frequency mutations, based on the accumulation of DNA damage.

Evolutionary forces promote bacterial growth in many environmental niches, so survival and growth under difficult conditions is crucial. It is then not surprising that bacteria adapt to their environment via the acquisition of novel genes via phages. Our results show that the release of chromosome-encoded phage proteins into the extracellular milieu causes a selective disadvantage to *B. cereus*, and the introduction of pBClin15 confers beneficial phenotypes that allow the exploitation of a competitive environment. We thus conclude that the capacity of *B. cereus* ATCC14579 to adapt to various environments arises in some cases from the acquisition of pBClin15. Finally, these data support the idea that pBClin15 may have a much greater role in *B. cereus* ecology than has hitherto been suspected.

Supplementary data to this article can be found online at http://dx.doi.org/10.1016/j.jprot.2016.06.022.

Conflicts of interest

The authors declare that *there are no conflicts of interest.*

Journal of Proteomics (2016), Vol. 146, p. 25-33, DOI: 10.1016/j.jprot.2016.06.022
Journal homepage : www.elsevier.com/locate/jprot

Acknowledgements

We thank Virginie Jouffrey for her help in proteomic data editing.

References

[1] M.H. Guinebretiere, S. Auger, N. Galleron, M. Contzen, B. De Sarrau, M.L. De Buyser, et al., *Bacillus cytotoxicus* sp. nov. is a novel thermotolerant species of the *Bacillus cereus* group occasionally associated with food poisoning, Int. J. Syst. Evol. Microbiol. 63 (2013) 31–40.
[2] G. Jimenez, M. Urdiain, A. Cifuentes, A. Lopez-Lopez, A.R. Blanch, J. Tamames, et al., Description of *Bacillus toyonensis* sp. nov., a novel species of the *Bacillus cereus* group, and pairwise genome comparisons of the species of the group by means of ANI calculations, Syst. Appl. Microbiol. 36 (2013) 383–391.
[3] J. Zheng, Z. Guan, S. Cao, D. Peng, L. Ruan, D. Jiang, et al., Plasmids are vectors for redundant chromosomal genes in the *Bacillus cereus* group, BMC Genomics 16 (2015) 6.
[4] D.A. Rasko, M.J. Rosovitz, O.A. Okstad, D.E. Fouts, L. Jiang, R.Z. Cer, et al., Complete sequence analysis of novel plasmids from emetic and periodontal *Bacillus cereus* isolates reveals a common evolutionary history among the *B. cereus*-group plasmids, including *Bacillus anthracis* pXO1, J. Bacteriol. 189 (2007) 52–64.
[5] M. Ehling-Schulz, B. Svensson, M.H. Guinebretiere, T. Lindback, M. Andersson, A. Schulz, et al., Emetic toxin formation of *Bacillus cereus* is restricted to a single evolutionary lineage of closely related strains, Microbiology 151 (2005) 183–197.
[6] T.M. Koehler, *Bacillus anthracis* genetics and virulence gene regulation, Curr. Top. Microbiol. Immunol. 271 (2002) 143–164.
[7] A. Aronson, Sporulation and delta-endotoxin synthesis by *Bacillus thuringiensis*, Cell. Mol. Life Sci. 59 (2002) 417–425.
[8] L.A. Bulla Jr., D.B. Bechtel, K.J. Kramer, Y.I. Shethna, A.I. Aronson, P.C. Fitz-James, Ultrastructure, physiology, and biochemistry of *Bacillus thuringiensis*, Crit. Rev. Microbiol. 8 (1980) 147–204.
[9] H.R. Whiteley, H.E. Schnepf, The molecular biology of parasporal crystal body formation in *Bacillus thuringiensis*, Annu. Rev. Microbiol. 40 (1986) 549–576.
[10] S. Guo, M. Liu, D. Peng, S. Ji, P. Wang, Z. Yu, et al., New strategy for isolating novel nematicidal crystal protein genes from *Bacillus thuringiensis* strain YBT-1518, Appl. Environ. Microbiol. 74 (2008) 6997–7001.
[11] C.R. Carlson, T. Johansen, A.B. Kolsto, The chromosome map of *Bacillus thuringiensis* subsp. Canadensis HD224 is highly similar to that of the *Bacillus cereus* type strain ATCC 14579, FEMS Microbiol. Lett. 141 (1996) 163–167.
[12] N. Ivanova, A. Sorokin, I. Anderson, N. Galleron, B. Candelon, V. Kapatral, et al., Genome sequence of *Bacillus cereus* and comparative analysis with *Bacillus anthracis*, Nature 423 (2003) 87–91.
[13] C. Verheust, N. Fornelos, J. Mahillon, GIL16, a new gram-positive tectiviral phage related to the *Bacillus thuringiensis* GIL01 and the *Bacillus cereus* pBClin15 elements, J. Bacteriol. 187 (2005) 1966–1973.
[14] H.W. Ackermann, W.A. Smirnoff, Study of lysogeny in *Bacillus thuringiensis* and *B. cereus*, Can. J. Microbiol. 24 (1978) 818–826.
[15] K.A. Bishop-Lilly, R.D. Plaut, P.E. Chen, A. Akmal, K.M. Willner, A. Butani, et al., Whole genome sequencing of phage resistant *Bacillus anthracis* mutants reveals an essential role for cell surface anchoring protein CsaB in phage AP50c adsorption, Virol. J. 9 (2012) 246.
[16] S. Sozhamannan, M. McKinstry, S.M. Lentz, M. Jalasvuori, F. McAfee, A. Smith, et al., Molecular characterization of a variant of *Bacillus anthracis*-specific phage AP50 with improved bacteriolytic activity, Appl. Environ. Microbiol. 74 (2008) 6792–6796.
[17] N.J. Stromsten, S.D. Benson, R.M. Burnett, D.H. Bamford, J.K. Bamford, The *Bacillus thuringiensis* linear double-stranded DNA phage Bam35, which is highly similar to the *Bacillus cereus* linear plasmid pBClin15, has a prophage state, J. Bacteriol. 185 (2003) 6985–6989.
[18] C. Verheust, G. Jensen, J. Mahillon, pGIL01, a linear tectiviral plasmid prophage originating from *Bacillus thuringiensis* serovar israelensis, Microbiology 149 (2003) 2083–2092.
[19] N. Fornelos, J.K. Bamford, J. Mahillon, Phage-borne factors and host LexA regulate the lytic switch in phage GIL01, J. Bacteriol. 193 (2011) 6008–6019.
[20] F.B. Stabell, W. Egge-Jacobsen, P.A. Risoen, A.B. Kolsto, O.A. Okstad, ORF 2 from the *Bacillus cereus* linear plasmid pBClin15 encodes a DNA binding protein, Lett. Appl. Microbiol. 48 (2009) 51–57.
[21] A. Voros, R. Simm, J.K. Kroeger, A.B. Kolsto, Gene transcription from the linear plasmid pBClin15 leads to cell lysis and extracellular DNA-dependent aggregation of *Bacillus cereus* ATCC 14579 in response to quinolone-induced stress, Microbiology 159 (2013) 2283–2293.
[22] J.P. Madeira, B. Alpha-Bazin, J. Armengaud, C. Duport, Time dynamics of the *Bacillus cereus* exoproteome are shaped by cellular oxidation, Front. Microbiol. 6 (2015) 342.
[23] E. Rosenfeld, C. Duport, A. Zigha, P. Schmitt, Characterization of aerobic and anaerobic vegetative growth of the food-borne pathogen *Bacillus cereus* F4430/73 strain, Can. J. Microbiol. 51 (2005) 149–158.
[24] G. Clair, J. Armengaud, C. Duport, Restricting fermentative potential by proteome remodeling: an adaptative strategy evidenced in *Bacillus cereus*, Mol. Cell Proteomics 11 (2012), M111 013102.
[25] G. Clair, S. Roussi, J. Armengaud, C. Duport, Expanding the known repertoire of virulence factors produced by *Bacillus cereus* through early secretome profiling in three redox conditions, Mol. Cell. Proteomics 9 (2010) 1486–1498.
[26] A. de Groot, R. Dulermo, P. Ortet, L. Blanchard, P. Guerin, B. Fernandez, et al., Alliance of proteomics and genomics to unravel the specificities of Sahara bacterium *Deinococcus deserti*, PLoS Genet. 5 (2009), e1000434.
[27] A. Dedieu, J.C. Gaillard, T. Pourcher, E. Darrouzet, J. Armengaud, Revisiting iodination sites in thyroglobulin with an organ-oriented shotgun strategy, J. Biol. Chem. 286 (2011) 259–269.
[28] J.P. Madeira, H. Omer, B. Alpha-Bazin, J. Armengaud, C. Duport, Cellular and Exoproteome Dynamics of *Bacillus cereus* ATCC 14579 with and Without pBClin15. Data in Brief, 2016 (Submitted).
[29] V. Dupierris, C. Masselon, M. Court, S. Kieffer-Jaquinod, C. Bruley, A toolbox for validation of mass spectrometry peptides identification and generation of database: IRMa, Bioinformatics 25 (2009) 1980–1981.
[30] B.L. Zybailov, L. Florens, M.P. Washburn, Quantitative shotgun proteomics using a protease with broad specificity and normalized spectral abundance factors, Mol. BioSyst. 3 (2007) 354–360.
[31] R. Suzuki, H. Shimodaira, Pvclust: an R package for assessing the uncertainty in hierarchical clustering, Bioinformatics 22 (2006) 1540–1542.
[32] A.C. Culhane, J. Thioulouse, G. Perriere, D.G. Higgins, MADE4: an R package for multivariate analysis of gene expression data, Bioinformatics 21 (2005) 2789–2790.
[33] M.B. Eisen, P.T. Spellman, P.O. Brown, D. Botstein, Cluster analysis and display of genome-wide expression patterns, Proc. Nat. Acad. Sci. U.S.A. 95 (1998) 14863–14868.
[34] G.K. Smyth, J. Michaud, H.S. Scott, Use of within-array replicate spots for assessing differential expression in microarray experiments, Bioinformatics 21 (2005) 2067–2075.
[35] J. Cox, M. Mann, MaxQuant enables high peptide identification rates, individualized p.p.b.-range mass accuracies and proteome-wide protein quantification, Nat. Biotechnol. 26 (2008) 1367–1372.
[36] J. Cox, N. Neuhauser, A. Michalski, R.A. Scheltema, J.V. Olsen, M. Mann, Andromeda: a peptide search engine integrated into the MaxQuant environment, J. Proteome Res. 10 (2011) 1794–1805.
[37] J. Cox, M.Y. Hein, C.A. Luber, I. Paron, N. Nagaraj, M. Mann, Accurate proteome-wide label-free quantification by delayed normalization and maximal peptide ratio extraction, termed MaxLFQ, Mol. Cell. Proteomics 13 (2014) 2513–2526.
[38] S. Castano-Cerezo, J.M. Pastor, S. Renilla, V. Bernal, J.L. Iborra, M. Canovas, An insight into the role of phosphotransacetylase (pta) and the acetate/acetyl-CoA node in *Escherichia coli*, Microb. Cell Factories 8 (2009) 54.
[39] K. Peebo, K. Valgepea, R. Nahku, G. Riis, M. Oun, K. Adamberg, et al., Coordinated activation of PTA-ACS and TCA cycles strongly reduces overflow metabolism of acetate in *Escherichia coli*, Appl. Microbiol. Biotechnol. 98 (2014) 5131–5143.
[40] M.R. Sadykov, V.C. Thomas, D.D. Marshall, C.J. Wenstrom, D.E. Moormeier, T.J. Widhelm, et al., Inactivation of the Pta-AckA pathway causes cell death in *Staphylococcus aureus*, J. Bacteriol. 195 (2013) 3035–3044.
[41] M.P. Brynildsen, J.A. Winkler, C.S. Spina, I.C. MacDonald, J.J. Collins, Potentiating antibacterial activity by predictably enhancing endogenous microbial ROS production, Nat. Biotechnol. 31 (2013) 160–165.
[42] J. Armengaud, J.A. Christie-Oleza, G. Clair, V. Malard, C. Duport, Exoproteomics: exploring the world around biological systems, Expert Rev Proteomics. 9 (2012) 561–575.
[43] E.M. Hartmann, F. Allain, J.C. Gaillard, O. Pible, J. Armengaud, Taking the shortcut for high-throughput shotgun proteomic analysis of bacteria, Methods Mol. Biol. 1197 (2014) 275–285.
[44] H. Omer, B. Alpha-Bazin, J.L. Brunet, J. Armengaud, C. Duport, Proteomics identifies *Bacillus cereus* EntD as a pivotal protein for the production of numerous virulence factors, Front. Microbiol. 6 (2015) 1004.
[45] S. GK, Linear models and empirical Bayes methods for assessing differential expression in microarray experiments, Stat. Appl. Genet. Mol. Biol. 3 (2004), Article3.
[46] E. Ravasz, A.L. Somera, D.A. Mongru, Z.N. Oltvai, A.L. Barabasi, Hierarchical organization of modularity in metabolic networks, Science 297 (2002) 1551–1555.
[47] A. Veit, T. Polen, V.F. Wendisch, Global gene expression analysis of glucose overflow metabolism in *Escherichia coli* and reduction of aerobic acetate formation, Appl. Microbiol. Biotechnol. 74 (2007) 406–421.
[48] K. Zhuang, G.N. Vemuri, R. Mahadevan, Economics of membrane occupancy and respiro-fermentation, Mol. Syst. Biol. 7 (2011) 500.
[49] M.D. Rolfe, C.J. Rice, S. Lucchini, C. Pin, A. Thompson, A.D. Cameron, et al., Lag phase is a distinct growth phase that prepares bacteria for exponential growth and involves transient metal accumulation, J. Bacteriol. 194 (2012) 686–701.
[50] K.J. Adolfsen, M.P. Brynildsen, Futile cycling increases sensitivity toward oxidative stress in *Escherichia coli*, Metabolic engineering. 29 (2015) 26–35.
[51] B. Gummesson, L.U. Magnusson, M. Lovmar, K. Kvint, O. Persson, M. Ballesteros, et al., Increased RNA polymerase availability directs resources towards growth at the expense of maintenance, EMBO J. 28 (2009) 2209–2219.
[52] T. Nystrom, Growth versus maintenance: a trade-off dictated by RNA polymerase availability and sigma factor competition? Mol. Microbiol. 54 (2004) 855–862.
[53] Y. Fujita, T. Satomura, S. Tojo, K. Hirooka, CcpA-mediated catabolite activation of the *Bacillus subtilis* ilv-leu operon and its negation by either CodY- or TnrA-mediated negative regulation, J. Bacteriol. 196 (2014) 3793–3806.
[54] C. Chiang, C. Bongiorni, M. Perego, Glucose-dependent activation of *Bacillus anthracis* toxin gene expression and virulence requires the carbon catabolite protein CcpA, J. Bacteriol. 193 (2011) 52–62.
[55] A.V. Toms, A.L. Haas, J.H. Park, T.P. Begley, S.E. Ealick, Structural characterization of the regulatory proteins TenA and TenI from *Bacillus subtilis* and identification of TenA as a thiaminase II, Biochemistry 44 (2005) 2319–2329.